Local Maximal Homogeneous Region Search for SAR Speckle Reduction With Sketch-Based Geometrical Kernel Function

Jie Wu, Fang Liu, *Senior Member, IEEE*, Licheng Jiao, *Senior Member, IEEE*, Xiangrong Zhang, *Member, IEEE*, Hongxia Hao, *Member, IEEE*, and Shuang Wang, *Member, IEEE*

***Abstract*—With the flourish of the nonlocal mean method, the neighborwise similarity metric is widely applied in speckle reduction for its robust performance on the search of similar samples. In this metric, an isotropic kernel function is usually chosen to aggregate the corresponding pixels' distance between two neighborhoods. It means that the kernel function is considered as the explanation of the local spatial relationship at each pixel. However, for anisotropic features (such as edges and lines), a strong relationship exists along their directions rather than across them, so the isotropic kernel is not suitable to explain the spatial relationship around these features. Meanwhile, due to the inherent speckle in synthetic aperture radar (SAR) images, the discrimination and exploration of the geometrical properties of anisotropic features are important for the construction of adaptive kernel function. In this paper, the sketch map which is a representation of the sketch information of SAR images is extracted as the criterion for designing the kernel function. Meanwhile, due to the properties of symmetric and maximal self-similarity, a modified ratio distance is proposed and used jointly with the constructed kernel function as a similarity metric. Then, under the local stationary assumption, the local maximal homogeneous region of each pixel is searched by using the region growing method with the proposed metric. Moreover, maximal likelihood rule is used within the region for the estimation of true value. From the experiments on the synthetic and real SAR images, a promising performance in terms of speckle reduction and preservation of the details is achieved by our proposed method.**

***Index Terms*—Geometrical kernel function, patch-based similarity, sketch map, synthetic aperture radar (SAR) speckle reduction.**

Manuscript received June 5, 2013; revised October 28, 2013; accepted November 15, 2013. Date of publication January 2, 2014; date of current version May 1, 2014. This work was supported by the National Basic Research Program (973 Program) of China (No. 2013CB329402), the Fund for Foreign Scholars in University Research and Teaching Programs (the 111 Project; No. B07048), the Program for Cheung Kong Scholars and Innovative Research Team in University (No. IRT1170), the National Natural Science Foundation of China (No. 61072106, 61173090, 61173092, 61271302, and 61272282), the Program for New Century Excellent Talents in University (No. NCET-11-0692), the Program for New Scientific and Technological Star of Shaanxi Province (No. 2013KJXX-64), the National Research Foundation for the Doctoral Program of Higher Education of China (No. 20110203110006), and the Fundamental Research Funds for the Central Universities (K5051203002 and K50511020011).

J. Wu, F. Liu, and H. Hao are with the School of Computer Science and Technology and also with the Key Laboratory of Intelligent Perception and Image Understanding of Ministry of Education of China, Xidian University, Xi'an 710071, China (e-mail: 607wujie2005@163.com; f63liu@163.com; chilamhaohao@163.com).

L. Jiao, X. Zhang, and S. Wang are with the Key Laboratory of Intelligent Perception and Image Understanding of Ministry of Education of China, Xidian University, Xi'an 710071, China (e-mail: lchjiao@mail.xidian.edu.cn; xrzhang@mail.xidian.edu.cn; shwang.xd@gmail.com).

Color versions of one or more of the figures in this paper are available online at http://ieeexplore.ieee.org.

Digital Object Identifier 10.1109/TGRS.2013.2292081

I. Introduction

Due to the acquisition under all weather conditions and all times, synthetic aperture radar (SAR) imagery plays an irreplaceable role on the study and analysis in many fields nowadays, such as ocean, agriculture, geology, etc. [1]. However, the granular speckle which is inherent in the coherent imaging system hinders the further utilization of the SAR image in these fields. Therefore, speckle reduction is one important preparation in SAR image processes.

Many speckle-filtering methods have been developed in the past decades, such as Lee filter [2], Kuan filter [3], Frost filter [4], gamma MAP filter [5], and so on. In these classical filtering methods, the assumption of the local stationary random process is used, and the true signal of interest is estimated according to the statistic information in its square neighboring region. However, this assumption is invalid in the neighborhoods containing the details (e.g., edges and lines), and the details are always being smeared in the results. It means that the determination of the regions satisfying the stationary assumption is very important for speckle reduction. In the literature [6]–[11], by using region division, the nonuniform regions containing the details are decomposed into a set of uniform subregions. Therefore, the stationary assumption becomes valid in the subregions, and classical filtering methods are reasonable to be applied for speckle reduction. In [6], the predefined neighborhood (window) containing the details was bisected into partially overlapped subregions by using different methods, and then, the subregion which was more homogeneous and had the largest difference with its opposite was chosen to estimate the true value of the central pixel. In [7] and [8], given a distribution of the neighbor pixels, only the valid pixels were chosen to estimate the true value of the central pixel. Since similar samples are only used in the estimation, the details are also well preserved by these filtering methods. However, due to the strong effect of multiplicative speckle in the SAR data, more similar samples are needed for a better reduction of speckle. In [9] and [10], according to the variation of the statistical property of the obtained region in the searching process, a local maximal rectangular window was determined for each pixel, and then, all pixels in the region were used for its estimation. In [11], with the usage of a pixel-based similarity metric, two-stage region growing method was used to determine the local maximal homogeneous region for each pixel, and the mean of all pixels in the region was used as the estimation. However, in some cases, the region could not grow properly owing to the strong effect of multiplicative speckle. This leads to the existence of some unexpected spots in the visual results [12]. At the same period, many multiresolution decomposition tools were applied in speckle reduction [13], [14] due to the successful applications of the multiresolution analysis methods on the nonstationary cases. Moreover, Markov Random Field [15], [16], PDE [17], and sparse representation [18] methods have been studied and applied in the reduction of speckle.

Recently, inspired by the nonlocal mean (NLM) filtering method proposed by Buades *et al.* [19], NLM-based despeckle methods are flourishing [20]–[22], in which the pixels' similarity is calculated according to the distance between their neighborhoods. In [20], with the weighted maximal likelihood estimation scheme, a pixelwise filtering method was developed for the reduction of speckle, in which the corresponding neighborhoods' distance was calculated as the combination of the noisy patches' distance and the corresponding current-calculated patches' distance. In [21], with the assumption that the corrupted multiplicative noise obeys the Gaussian distribution, Pearson distance and blockwise estimation method were jointly used to suppress the noise. Since the neighborhood of a pixel contains more information than itself, it is more credible to calculate the pixels' similarity according to their neighborhoods than that computed only by themselves. In other words, the neighborwise metric is more reliable and interpretable to estimate the similarity of noisy samples. In order to obtain an approximated unbiased metric, a kernel function is usually used for the interpretation of the spatial relationship in the neighborhood [19]. It means that the kernel function exposes the contribution of different neighboring pixels to the similarity metric. Therefore, the local spatial relationship should be carefully explored and exploited in the construction of kernel function, especially for the pixels around the details (such as edges and lines). Due to the directionality of edges and lines, a larger weight should be set along their directions rather than across them. In other words, the local geometrical orientation should be embodied in the constructed kernel function for the pixels nearby the details. However, owing to the destructive and constructive effects of speckle, the discrimination of the regions containing the details and the calculation of the local geometrical parameter are two main issues for the robust construction of kernel function. This procedure is very similar to that of [23] in which the regions containing the details were discriminated by using the coefficient of variance (CV) and a kernel function was constructed adaptively by using the structure tensor method. Then, with the kernel function as the weighting method, a weighted Lee filter was used for estimation. In this paper, owing to the consideration of local geometrical property, the constructed kernel function is named as the geometrical kernel function.

Inspired by the issues represented previously, the sketch information which is recorded as the sketch map is extracted from the SAR image for the discrimination of the structural and nonstructural portions. Since the sketch map is considered as a concise representation of the structural information of an image, more details (e.g., edges and lines) are contained in the obtained structural portion. Meanwhile, the orientations of these details are also calculated in the sketching process. Therefore, the geometrical kernel function which is constructed according to the extracted sketch map is suitable to represent the local geometrical spatial relationship. Moreover, a modified ratio distance is developed for its properties of symmetric and maximal self-similarity. Then, by combing the modified ratio distance and the geometrical kernel function, the region growing method is used in our method to determine the local maximal homogeneous region of each pixel. This procedure is very similar to that of [24], in which the ratio-based relative metric and eight-direction searching method were used to determine the local maximal homogeneous region for each pixel.

The rest of this paper is organized as follows. Section II presents the sketching process of SAR image with the edge-line detectors and hypothesis testing. In Section III, the geometrical kernel function is constructed by exploiting the extracted sketch information and is used to determine the local maximal homogeneous region of each pixel by combining with the modified ratio distance. Then, maximal likelihood rule (ML) is used within the obtained region for estimating the underlying signal. In Section IV, the experiments with synthetic and real SAR images are done and analyzed. Finally, the conclusion is made in Section V.

II. Sketch Map of SAR Image

In this section, according to the multiplicative speckle characteristic of SAR image, the sketching method for SAR images is given in detail. In this method, the ratio-based, cross-correlation-based, and gradient-based edge-line detectors are used together for the detection of edge-line features, and a hypothesis-testing method is used sequentially to make a selection on the extracted lines. Then, a meaningful sketch map is obtained by retaining the significant lines.

A. *Speckle Model*

Under the assumption of fully developed speckle in SAR image, the probability density function (pdf) of a multilook amplitude image follows the Nakagami–Rayleigh distribution [20] which is shown as

$$P_A(A|\delta) = \frac{2}{\Gamma(L)}\left(\frac{L}{\delta}\right)^L A^{2L-1}e^{-\frac{LA^2}{\delta}}, (A \geq 0) \qquad (1)$$

where A denotes the observed amplitude SAR image, L represents the number of looks, and δ indicates the backscattering coefficient.

According to [25], the speckle of a SAR image is modeled as the multiplicative noise, so the relationship among the speckle, the observed intensity, and the true value is shown as

$$Y = X \cdot S \qquad (2)$$

where Y indicates the observed intensity, S is the speckle, and X represents the underlying signal that is equal to $\sqrt{\delta}$ for the amplitude SAR image.

B. Extraction of Sketch Line

Since the sketch map is considered as a concise representation of the structural information contained in an image [26], the edge and line detectors are both needed for the extraction of sketch lines [27]. Meanwhile, due to the corruption with the multiplicative speckle, the sketching method proposed in [27] is invalid for the SAR image.

Recently, many methods have been proposed for the edge detection in a SAR image [28]–[30], in which the property of the speckle in a SAR image is taken into account and the scheme of constant false alarm rate (CFAR) is designed. In our method, two classical detectors (ratio-based detector (RoA) [28] and cross-correlation-based detector (CC) [32]) are fused for the detection of edge-line features in a SAR image. For the line detection, since the line can be modeled as two close and parallel edges in which a common part exists, the line detection method can be designed by employing the edge detection method twice [31]. It means that the whole template is divided into two one-pixel spaced regions for edge detection, while the line template consists of three regions.

The edge and line responses of the RoA detector are computed as follows:

$$R_{\text{edge}(i,j)} = 1 - \min\left\{\frac{\hat{\mu}_i}{\hat{\mu}_j}, \frac{\hat{\mu}_j}{\hat{\mu}_i}\right\} \tag{3a}$$

$$R_{\text{line}(i,j,q)} = \min\left\{R_{\text{edge}(i,j)}, R_{\text{edge}(j,q)}\right\} \tag{3b}$$

where $\hat{\mu}_k$ represents the mean value of region k, $R_{\text{edge}(i,j)}$ represents the RoA-based edge response between regions i and j, and $R_{\text{line}(i,j,q)}$ indicates the RoA-based line response among three ordered regions i, j, and q. From the definitions shown in (3), we can find that the RoA-based edge and line responses lie in the interval [0, 1], and the larger the calculated response, the higher the probability of the existence of an edge-line feature. However, the response of the RoA detector is prune to be influenced by an isolated point [31]. Therefore, the CC detector, which is also a CFAR detector [31], is employed in our method for the detection of edge-line features. The corresponding edge and line responses are computed as follows:

$$C_{\text{edge}(i,j)} = \sqrt{\frac{1}{1 + (N_i + N_j)\frac{N_i S_i^2 + N_j S_j^2}{N_i N_j (\hat{\mu}_i - \hat{\mu}_j)^2}}} \tag{4a}$$

$$C_{\text{line}(i,j,q)} = \min\left\{C_{\text{edge}(i,j)}, C_{\text{edge}(j,q)}\right\} \tag{4b}$$

where N_k, S_k, and $\hat{\mu}_k$ represent the number of pixels, the standard deviation, and the mean in region k, respectively, $C_{\text{edge}(i,j)}$ represents the CC-based edge response between regions i and j, and $C_{i,j,q}$ indicates the CC-based line response among three ordered regions i, j, and q. From (4), we can see that the responses of CC-based edge and line detectors are also in the range [0, 1]. Since the statistical information of each part in the templates is used for the calculation, the responses of CC detectors are more coherent than those of RoA detectors.

From the definitions shown in (3) and (4), we can find that these detectors are only suitable for the detection of monoedge and monoline cases. Therefore, the weighting method and the multiscale multiorientation detection method are jointly used in our method for an effective detection of edge-line features. Due to the directionality of the edge-line features, an anisotropic Gaussian kernel whose orientation is consistent with the corresponding template is chosen as the weighting map in our method. The templates and the corresponding kernels used in our method are shown in Fig. 1. It is noted that 3 scales and 18 directions are used, while the kernels' elongation factor is set as 2 according to the designed templates.

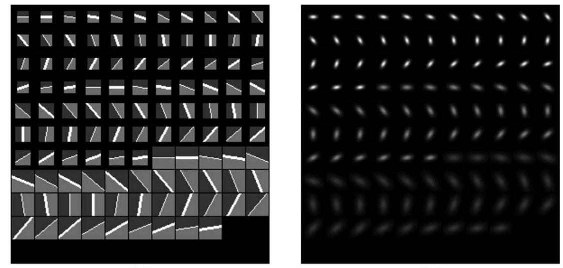

(a) (b)

Fig. 1. Templates and weighting maps. (a) Templates for edge and line detection. It is noted that one pixel is spaced between the two regions which constitute the edge templates, while the width of the middle part in the line templates is set as three pixels. (b) Weighting maps corresponding to the templates in (a).

By using these methods, the CFAR thresholds on the weighted responses of RoA and CC are very difficult to be estimated. It means that the method used in [31] is hardly to be applied to fuse the responses of RoA and CC detectors. However, since these two detectors are all CFAR detectors and the ranges of their responses are the same, a simple mean fusion operation $\sqrt{(R^2 + C^2)/2}$ [33] is chosen in our method to combine their responses for each template. Meanwhile, due to the usage of the weighting method, it is feasible to make the direct comparison between the responses of different templates. Therefore, the largest response among all templates is selected as the best response, and corresponding orientation is recorded as the local dominant orientation. It is noted that the weighting coefficient is normalized in each part of the template. Therefore, the computing method for the CC-based edge response is changed into (5) in which the factors indicating the number of pixels in each part of the template are eliminated

$$C_{\text{edge}(i,j)} = \sqrt{\frac{1}{1 + 2\frac{S_i^2 + S_j^2}{(\hat{\mu}_i - \hat{\mu}_j)^2}}}. \tag{5}$$

Then, the intensity map is obtained, and the edge-line point can be simply determined by using a threshold on the intensity map. Moreover, for a true edge-line feature, its gradient value should also be larger than a threshold [29]. Although the gradient information is not suitable for the edge-line detection in SAR image, some important discriminative information is really contained in the gradient map. Therefore, the gradient information is also calculated as the criterion for differentiating the true edge-line features in our method. The gradient-based edge and line responses are, respectively, computed as follows:

$$\text{Grad}_{\text{edge}(i,j)} = \|\hat{\mu}_i - \hat{\mu}_j\| \tag{6a}$$

$$\text{Grad}_{\text{line}(i,j,q)} = \min\left\{\text{Grad}_{\text{edge}(i,j)}, \text{Grad}_{\text{edge}(j,q)}\right\} \tag{6b}$$

where $\hat{\mu}_k$ indicates the weighted mean of region k, $\mathrm{Grad}_{\mathrm{edge}(i,j)}$ represents the gradient-based edge response between regions i and j, and $\mathrm{Grad}_{i,j,q}$ is the gradient-based line response among three ordered regions i, j, and q. It is noted that the gradient response at a pixel is computed by using the template that gives the best intensity response at the pixel. When the gradient response at each pixel is calculated, a gradient map is obtained.

With a proper fusion of the intensity map and the gradient map, a better discrimination of the true edge-line features can be achieved by the fused map. In our method, the operation (7) is chosen for the fusion of the two maps

$$f(x,y) = \frac{xy}{1-x-y+2xy}, \quad x,y \in [0,1] \tag{7}$$

where x and y indicate the corresponding values in the gradient map and the intensity map and $f(x,y)$ represents the fused strength. By using the operation, the fused value will be larger or smaller than the values to be fused if they are all larger or smaller than 0.5, while a compromised value is obtained for the rest of the cases [33]. Therefore, before the fusion, the two maps are both normalized into [0, 1] and shifted by $\max\{0, \min\{1, x - x_O + 0.5\}\}$. The values of x_O calculated, respectively, on the intensity map and the gradient map play the same role as the thresholds used in [29]. In our method, the calculation method proposed in [34] is chosen to estimate the value of x_O for the intensity map and the gradient map, in which the value is calculated by making a tradeoff on the distances of intraclass and interclass.

In the fusion process, an uncertain case will be caused when different decisions are obtained from the gradient response and the intensity response at a pixel. For better dealing with the uncertain pixels, the nonmax suppression and connection methods in Canny detection method [35] are used in our method to extract the lines which will be selected to construct the sketch map after the hypothesis testing. In this process, a heuristic method is chosen to make a decision for the uncertain pixels.

C. Selection of Sketch Lines

As a compact representation of the edge-line features in a SAR image, the elements of the sketch map should be significant and important. Therefore, the significance of each extracted line should be evaluated, and only the significant lines are preserved to form the sketch map. In this process, some false alarm lines are also removed.

In our method, a pair of paradoxical hypotheses is established for calculating the significance of each extracted line, which is shown as follows.

1) H_0: the extracted line cannot be preserved as the sketch line.
2) H_1: the extracted line can be preserved as the sketch line.

Similar with [27], each extracted line is approximated by a set of line segments, and its significance is calculated as

$$F = \sum_m \left(\ln P(B_m|H_1) - \ln P(B_m|H_0)\right) \tag{8}$$

where F stands for the significance of an extracted line which is constituted by line segments $\{B_m\}$, subscript m indicates that B_m is the mth line segment of the extracted line, and $P(B_m|H_i)$, $i \in \{0,1\}$ measures how the line segment B_m satisfied the hypothesis H_i according to its neighboring pixels. It is noted that the directionality of the local region is an important criterion in the calculation of F. It means that all pixels in the neighborhood are considered to be of the same true value for H_0, while only the neighboring pixels along the direction of the line segment are of the same true value for H_1. Due to the multiplicative speckle in the amplitude SAR image, $P(B_m|H_i)$, $i \in \{0,1\}$ is computed as follows:

$$\begin{aligned} & P(B_m|H_i) \\ &= \sum_{k=1}^{n} P(A_k|H_i) \\ &= \frac{2^n L^{nL}}{\Gamma(L)^n} \exp\left\{ \sum_{k=1}^{n} \left[-L\frac{A_k^2}{\hat{A}_k^2} + (2L-1)\ln\left(A_k^2\right) \right.\right. \\ &\qquad\qquad \left.\left. - L\ln\left(\hat{A}_k^2\right) \right] \right\} \\ &= \frac{2^n L^{nL}}{\Gamma(L)^n} \exp\left\{ -L\sum_{k=1}^{n} \left[\frac{A_k^2}{\hat{A}_k^2} - \left(2-\frac{1}{L}\right)\ln(A_k^2) \right.\right. \\ &\qquad\qquad \left.\left. + \ln(\hat{A}_k^2) \right] \right\} \\ &= \exp\left\{ -L\sum_{k=1}^{n} \left[\frac{A_k^2}{\hat{A}_k^2} - \left(2-\frac{1}{L}\right)\ln\left(A_k^2\right) + \ln\left(\hat{A}_k^2\right) \right] \right. \\ &\qquad \left. + C(n,L) \right\} \end{aligned} \tag{9}$$

where L is the number of looks, n represents the number of pixels in the neighborhood of the line segment B_m, A_k indicates the observed value of these pixels, $\hat{A}_k$ is the estimated value under the assumption of H_i, and $C(n,L)$ is a constant value which is only related to the number of pixels and the number of looks. Then, we can get

$$\ln P(B_m|H_i) \propto -\sum_{k=1}^{n} \left[\frac{A_k^2}{\hat{A}_k^2} - \left(2-\frac{1}{L}\right)\ln\left(A_k^2\right) + \ln\left(\hat{A}_k^2\right) \right]. \tag{10}$$

Substituting (10) in (8), the significance of an extracted line is computed. Based on the histogram of the significance of all extracted lines, a threshold is selected for the construction of the sketch map. It means that the lines whose significances are smaller than the selected threshold are not preserved in the sketch map. Since the selected threshold is related to the content of the image, different values will be chosen for different images. Usually, the value at the first peak of the histogram is chosen as the threshold.

In Fig. 2, a real SAR image is taken as an example, and its corresponding intensity map, fused strength map, orientation map, sketch map, and histogram map are, respectively, shown as Fig. 2(b)–(f). According to its histogram map, 5 is chosen as the threshold to select the significant lines. By comparing the intensity map and fused strength map, we can see that the edge-line features are more easily discriminated by using the latter.

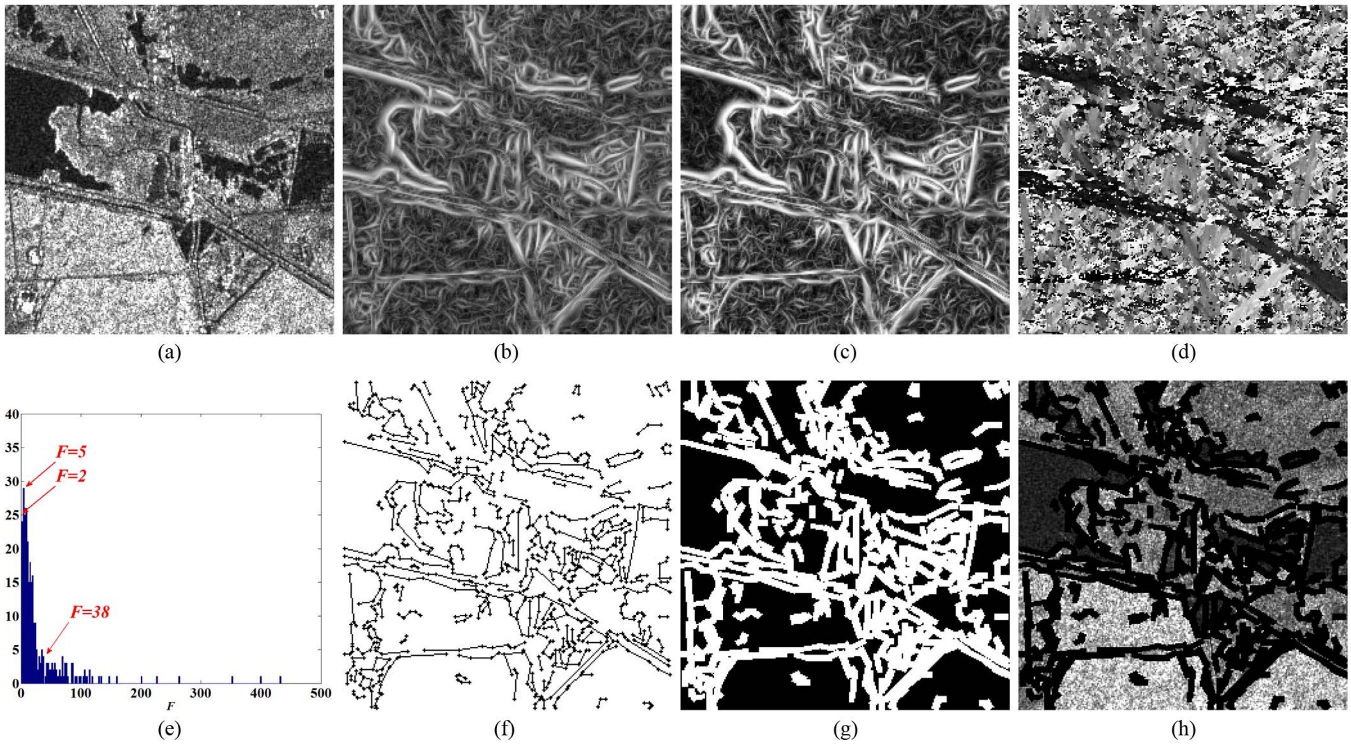

Fig. 2. (a) Real SAR image (estuary near Yellow River in China, C-band, 8-m resolution, four-look). (b) Intensity map. (c) Fused strength map. (d) Orientation map. (e) Histogram map on the significance of extracted lines. (f) Extracted sketch map in which end points of each line segment are marked as solid dot. (g) Binary map for the structural (white) and nonstructural (black) portions. (h) Pixels belong to the nonstructural portion.

III. Sketch-Based Geometrical Kernel Function for Speckle Reduction

In this section, according to the extracted sketch map, a geometrical kernel function is constructed adaptively for each pixel by combining the local geometrical property. Meanwhile, a modified ratio distance is developed for its properties of maximal self-similarity and symmetry. Then, a new neighborwise similarity metric is formed. Sequentially, the region growing method is chosen to find the local maximal homogeneous region with the proposed metric, and the ML rule is used within the obtained region to estimate the true value.

A. *Construction of Geometrical Kernel Function*

Since almost all anisotropic features are marked in the sketch map, a reasonable discrimination of structural and nonstructural portions can be achieved according to the extracted sketch map. Meanwhile, due to the multiscale and multiorientation scheme used in the sketching process, the geometrical properties implied by the sketch map are reasonable. Thus, the geometrical kernel function constructed according to the extracted sketch map is suitable to be used as the interpretation of local geometrical spatial relationship.

As explained in Section II-C, a sketch map can be considered as a composition of line segments. For a better discrimination of the structural and nonstructural portions of a SAR image, an oriented rectangular window is designed in our method for the extraction of the structural portion. It is noted that the window is constructed separately for each line segment and its long edge is aligned with the concerned line segment. The constructing method is shown as (11). According to the size of the templates used for the detection of edge-line features, the width and height of the constructed window are set as $s_l = 7$ and $s_w = 5$ in our algorithm.

$$W(\theta, x_0, y_0, s_l, s_w) = \Big\{(x, y) \mid \|f_1(x, y, x_0, y_0, \theta)\| \le \frac{s_l}{2}, \|f_2(x, y, x_0, y_0, \theta)\| \le \frac{s_w}{2}\Big\} \tag{11}$$

where (x_0, y_0) indicates the window's central point, (x, y) is a neighboring point of (x_0, y_0), θ represents the orientation of the window's long edge, s_l and s_w are, respectively, the window's height and width, $\|\cdot\|$ is the absolute operation, and the coupled rotation functions $f_1()$ and $f_2()$ are defined as follows:

$$\begin{cases} f_1(x, y, x_0, y_0, \theta) = -(y - y_0)\sin\theta + (x - x_0)\cos\theta \\ f_2(x, y, x_0, y_0, \theta) = (y - y_0)\cos\theta + (x - x_0)\sin\theta. \end{cases} \tag{12}$$

By aligning (x_0, y_0) with each point of the concerned line segment and labeling all pixels contained in the window, a region that contains the line segment is determined. In other words, all labeled pixels constitute the region that includes the feature represented by the line segment. When the region of each line segment is extracted, the structural portion of the whole image is determined, while the rest is the nonstructural portion. For a real SAR image [shown in Fig. 2(a)], the classified binary map and the corresponding nonstructural portion of a SAR image are shown, respectively, in Fig. 2(g) and (h), from which we can see that almost all edge-line features are included in the structural portion.

Since the constructed geometrical kernel functions in our method are essentially the Gaussian function, a universal formulation of these functions is given as follows:

$$\begin{aligned}&\mathrm{Kernel}_{(x_0,y_0)}(x,y)\\&=\exp\left\{-\frac{f_1^2(x,y,x_0,y_0,\theta)+\lambda^2 f_2^2(x,y,x_0,y_0,\theta)}{\sigma^2}\right\}\end{aligned} \quad (13)$$

where (x_0, y_0) indicates the interested pixel, (x, y) represents the neighboring pixel, θ and λ are, respectively, the orientation and the elongation factor of the kernel function, $f_1()$ and $f_2()$ are the rotation function defined as (12), and σ is the standard variance which indicates the local spatial relationship. From the definition, we can see that the geometrical kernel function is isotropic when $\theta = 0$ and $\lambda = 1$. It means that the geometrical kernel functions used in structural and nonstructural portions are only different in the orientation and the elongation factor. A larger value of λ indicates a higher ratio between the long axis and short axis. In our method, λ is experimentally set as 3 for the pixels in the structural portion.

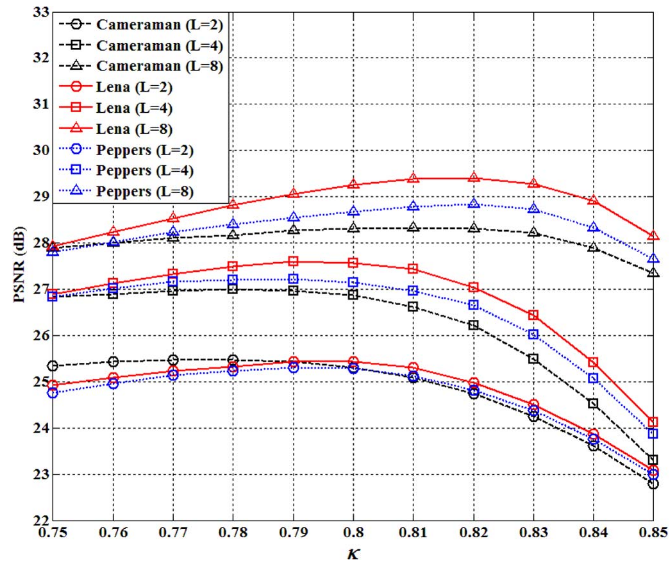

Fig. 3. Variation of the PSNR to different values of scale factor κ. The test images are Lena (256∗256), Cameraman (256∗256), and Peppers (256∗256).

B. Speckle Reduction With Local Homogeneous Region

Since the speckle in a SAR image is modeled as multiplicative noise, Euclidean metric is invalid in measuring the similarity between the speckled patches. In [24], a relative metric was proposed for measuring the similarity of two speckled patches, which was derived from the pdf of the ratio distance of two speckled pixels. However, from the curves of the distance to different looks of speckle [24], we can see that this metric does not have the properties of symmetric and maximal self-similarity. In our method, the ratio distance of two speckled values is modified as (14) for searching the similar samples

$$R(Y_i, Y_j) = \min\left\{\frac{Y_i}{Y_j}, \frac{Y_j}{Y_i}\right\} \quad (14)$$

where Y_i and Y_j indicate two noisy pixels whose similarity needs to be measured. From the definition, we can see that the properties of symmetric and maximal self-similarity are well satisfied by the proposed metric.

Then, by combining with the geometrical kernel function constructed in Section III-A, a new neighborwise similarity metric is defined as

$$\mathrm{Sim}(V_p, V_q) = \frac{\sum \mathrm{Kernel}_p(\cdot) R\left(V_p(\cdot), V_q(\cdot)\right)}{\sum \mathrm{Kernel}_p(\cdot)} \quad (15)$$

where $\mathrm{Kernel}_p(\cdot)$ indicates the geometrical kernel function that is constructed for the concerned pixel p and $V_k(\cdot)$ represents a neighbor pixel of pixel k.

The main steps of our algorithm are shown as follows.

1) Extracting the sketch map of the input SAR image.
2) Discriminating the structural and nonstructural portions according to the extracted sketch map.
3) For each pixel in the image, a geometrical kernel function is built by (13), and the neighborwise similarity metric [defined as (15)] is used in search of the local maximal homogeneous region. In essence, this procedure is a region growing process. For the computing efficiency of the algorithm, the obtained region is limited in a larger window centering on the concerned pixel in our method. In all experiments, the size of the window is set as 15.
4) With the obtained region, the ML rule is used for the estimation of the underlying signal.

C. Parameter for Region Growing

Since a region growing scheme is used in our method to determine the local maximal homogeneous region, a stop criterion is very important for the obtention of a larger and reasonable region. Moreover, due to a stronger effect of multiplicative speckle, the criterion is reasonable to be related to the levels of speckle. In [24], the threshold used to search the local maximal homogeneous region was proportional to the maximal value of the relative metric which varies with the levels of speckle. In our algorithm, the threshold is set to be proportional to the ratio value which is of the highest pdf. Thus, the value is calculated as follows:

$$Th = \kappa \cdot \sqrt{\frac{(2L-1)}{(2L+1)}} \quad (16)$$

where L stands for the number of looks which is an index of the level of speckle and κ is the scale factor.

In order to make a reasonable selection of the scale factor κ, three natural images (Lena, Peppers, and Cameraman) corrupted with different levels of speckle ($L = 2, 4,$ and 8) are used in the experiments, and the corresponding curves that represent the variation of the peak signal-to-noise ratio (PSNR) to different κ values are given in Fig. 3. From the curve chart, we can find that the scale factor κ has a significant effect on the estimated results. When the peak values of these curves are observed, the scale factor κ corresponding to the highest PSNR is in the interval [0.77, 0.83]. Obviously, a smaller scale factor κ will lead to a stronger reduction of speckle and is prone to be chosen for the data which are corrupted with more serious

(a) (b) (c)

Fig. 4. Three synthetic images. (a) Multimode. (b) Fiveclass. (c) Multicurve.

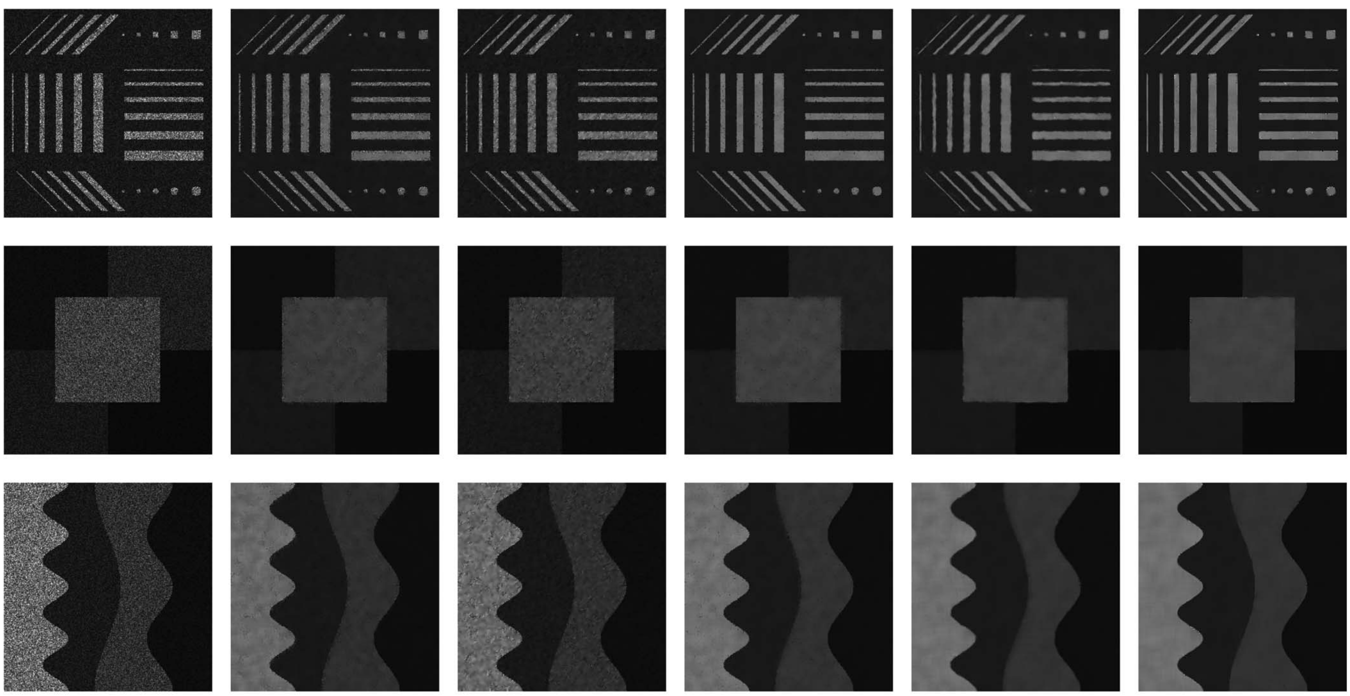

(a) (b) (c) (d) (e) (f)

Fig. 5. Results of synthetic images that are corrupted with two-look speckle. The first column shows the speckled images. From left to right are the results of (b) Refined Lee filter, (c) AKMMSE filter, (d) TSRG filter, (e) LHRS-PRM filter, and (f) our proposed filter.

speckle. Therefore, in our algorithm, the factor κ is set to be 0.77 when the level of speckle is $L \leq 4$; otherwise, $\kappa = 0.81$.

IV. Experiments

To check the effectiveness of our algorithm, three synthetic images and four real SAR images are used in the experiments. The comparison filtering methods include the Refined Lee filter [6], AKMMSE filter [23], TSRG filter [11], and LHRS-PRM filter [24]. The visual results and their corresponding numerical results are given for the qualitative and quantitative analyses. For the Refined Lee filter and AKMMSE filter, the size of the window is set to be 9, and the smoothing factor is set to be 1.4 for the AKMMSE filter. For the TSRG filter, the first and second stopping criteria are set to be 1.5 and 1.0, respectively, and the maximal number in the first region growing is set to be 100 for computational efficiency. The parameters of the LHRS-PRM filter are set according to [24]. At last, the time consumptions of our method on four real SAR images are given in detail.

A. Synthetic Images

The synthetic images (shown in Fig. 4) are corrupted with two different levels of speckle ($L = 2$ and 4) in the experiments, and the numerical indexes including the PSNR, mean of structural similarity index (MSSIM) [36], and edge preservation degree based on RoA (EPD-RoA) [24] are calculated for the quantitative analysis. It is noted that, due to the availability of the underlying signal, two full reference indexes (PSNR and MSSIM) are used for evaluation. For the two indexes, a larger value means a better performance on the restoration of the underlying signal (PSNR) or the structure property (MSSIM). For EPD-RoA, a higher value implies a better persistence of the details. The visual results are shown in Figs. 5 and 7, while the numerical indexes are calculated in Table I. It is noted that all speckled images are truncated into 8-bit images.

From the despeckled results of the Refined Lee filter and AKMMSE filter [shown as Fig. 5(b) and (c)], we can see that the details are well preserved by using the strategy of the region division (Refined Lee filter) or the local correlation analysis (AKMMSE filter). In essence, the local dominant orientation is

TABLE I
NUMERICAL INDEXES FOR SYNTHETIC IMAGES

	SSIM	PSNR	EPD-ROA		SSIM	PSNR	EPD-ROA	
			Horizonal	Vertical			Horizonal	Vertical
	Multimode(2L)				Multimode(4L)			
Refined Lee	0.8735	25.9105	0.8552	0.8554	0.9163	28.1518	0.9362	0.9367
AKMMSE	0.8321	26.2369	**0.8614**	**0.8619**	0.8948	28.7086	**0.9374**	**0.9379**
TSRG	0.9555	31.5528	0.8395	0.8405	0.9805	**37.0482**	0.9273	0.9284
LHRS-PRM	0.9261	28.5027	0.8296	0.8300	0.9542	30.8241	0.9134	0.9141
Proposed	**0.9691**	**31.7543**	0.8469	0.8467	**0.9868**	35.1742	0.9303	0.9307
	Fiveclass(2L)				Fiveclass(4L)			
Refined Lee	0.9262	34.5403	0.8493	0.8491	0.9552	37.9376	0.9322	0.9334
AKMMSE	0.8085	31.6715	**0.8583**	**0.8585**	0.8723	34.8037	**0.9362**	**0.9373**
TSRG	0.9583	39.5712	0.8463	0.8464	0.9659	41.9081	0.9310	0.9320
LHRS-PRM	0.9764	38.4985	0.8435	0.8436	0.9877	41.4650	0.9277	0.9291
Proposed	**0.9895**	**42.5758**	0.8474	0.8470	**0.9956**	**46.6709**	0.9302	0.9314
	Multicurve(2L)				Multicurve(4L)			
Refined Lee	0.8883	31.3439	0.8513	0.8518	0.9269	35.1324	0.9317	0.9322
AKMMSE	0.7200	27.9840	**0.8598**	**0.8599**	0.7991	30.9251	**0.9365**	**0.9364**
TSRG	0.9270	35.7824	0.8486	0.8485	0.9370	38.3930	0.9307	0.9307
LHRS-PRM	0.9606	34.6136	0.8462	0.8457	0.9717	35.6828	0.9276	0.9265
Proposed	**0.9768**	**36.7471**	0.8483	0.8483	**0.9869**	**38.9604**	0.9296	0.9292

calculated for the concerned pixel and used implicitly to determine the efficiency of its neighboring pixels for the estimation in both of these two methods. However, some speckle residual is clearly observed in their visual results. The main reason is that a predefined window is used in these two methods. It means that the valid samples used to estimate the true value are not enough. In the AKMMSE filter, for an effective calculation of the local morphology by the structural tensor method, the CV is applied to discriminate the regions containing the details. Since the CV is computed in a window, its performance is very sensitive to the size of the window. Thus, the results of the AKMMSE filter look noisier than that of the Refined Lee filter. By using the region growing method, the speckle is greatly reduced, and many details are well preserved in the results of the TSRG filter [shown as Fig. 5(d)]. With a careful observation, we can find that many unexpected dark spots appear in the results. It is because a smaller region is usually obtained by using the pixel-based similarity for the pixel which is affected seriously by speckle. For the LHRS-PRM filter, with the usage of the neighborwise similarity metric, not only the speckle is reduced greatly, but also the details are well preserved in the results [shown as Fig. 5(e)]. Moreover, the unexpected spots are eliminated. It is because the risk of the larger deviation for a single pixel is reduced by using the neighborwise similarity metric, and more valid similar samples are searched for the estimation, whereas due to the lack of the analysis of the local geometrical property, the profiles of the details are not well restored in the results of the LHRS-PRM filter, especially for the weak details [shown as the bottom-left and top-right edges in the result of Fiveclass and the middle curve in the result of Multicurve in Fig. 5(e)]. From the visual results of the proposed filter [shown as Fig. 5(f)], we can find that a better preservation of details is obtained, while the speckle is reduced largely. This is because the neighborwise similarity metric and the geometrical kernel function constructed by exploiting the extracted sketch information are jointly used to determine the local maximal homogeneous region of each pixel. In other words, the analysis of the local morphology is very important for the restoration of underlying signal, especially for the details.

For a further analysis, the local profiles restored from two-look speckled Multimode by these filtering methods are shown in Fig. 6, which correspond to the profile marked by white line shown in Fig. 4(a). From Fig. 6, we can find that the maximal deviation is the smallest in the result of our method. With a careful observation, we can see that the deviation nearby each step profile is smaller in the result of our method than in the result of the LHRS-PRM filter. It means that a better approximation to the original step profile is achieved by the proposed method. Similar conclusions can also be obtained for the synthetic images corrupted with four-look speckle, whose visual results are shown in Fig. 7.

In Table I, the numerical indexes (including MSSIM, PSNR, and EPD-RoA) of the visual results are listed for the quantitative analysis where the best values are marked in bold. From the table, we can see that the highest value in terms of MSSIM is obtained by the proposed method among all comparison methods, while the PSNR of our method is only inferior to the TSRG filter for Multimode corrupted with four-look speckle. In terms of EPD-RoA, due to the existence of speckle residual, a higher value is achieved by the AKMMSE filter and Refined

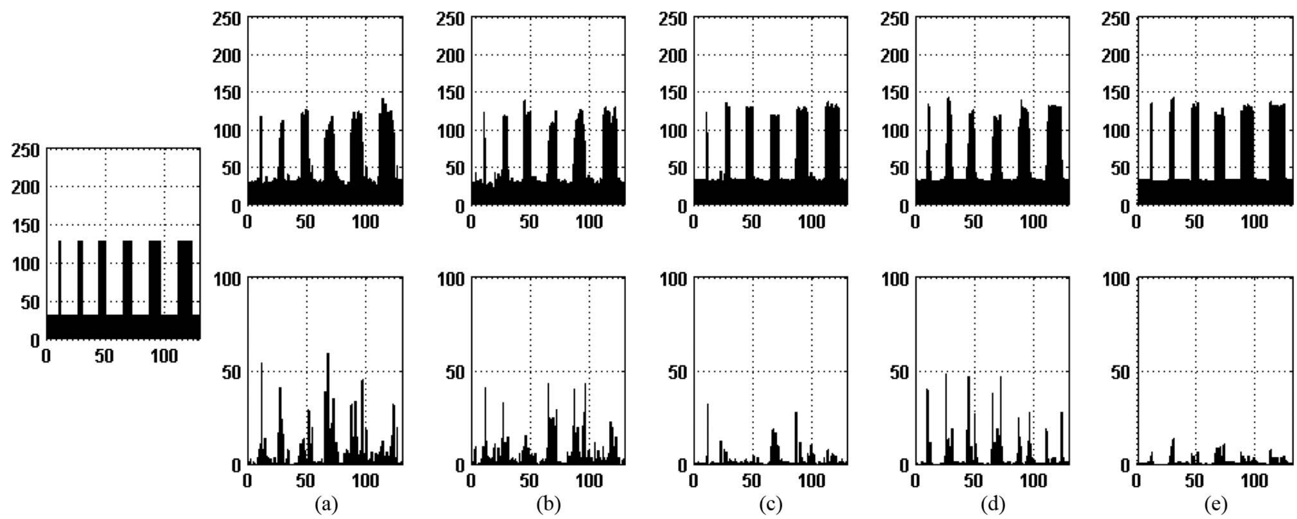

Fig. 6. Despeckled profiles corresponding to the profile marked in Fig. 4(a) and corrupted with two-look speckle. The first column is the underlying profile. For the rest, the first row is the restored profiles, and the second row is the deviation of the restored to the underlying. From left to right, the profiles are the results of (a) Refined Lee filter, (b) AKMMSE filter, (c) TSRG filter, (d) LHRS-PRM filter, and (e) Our proposed filter.

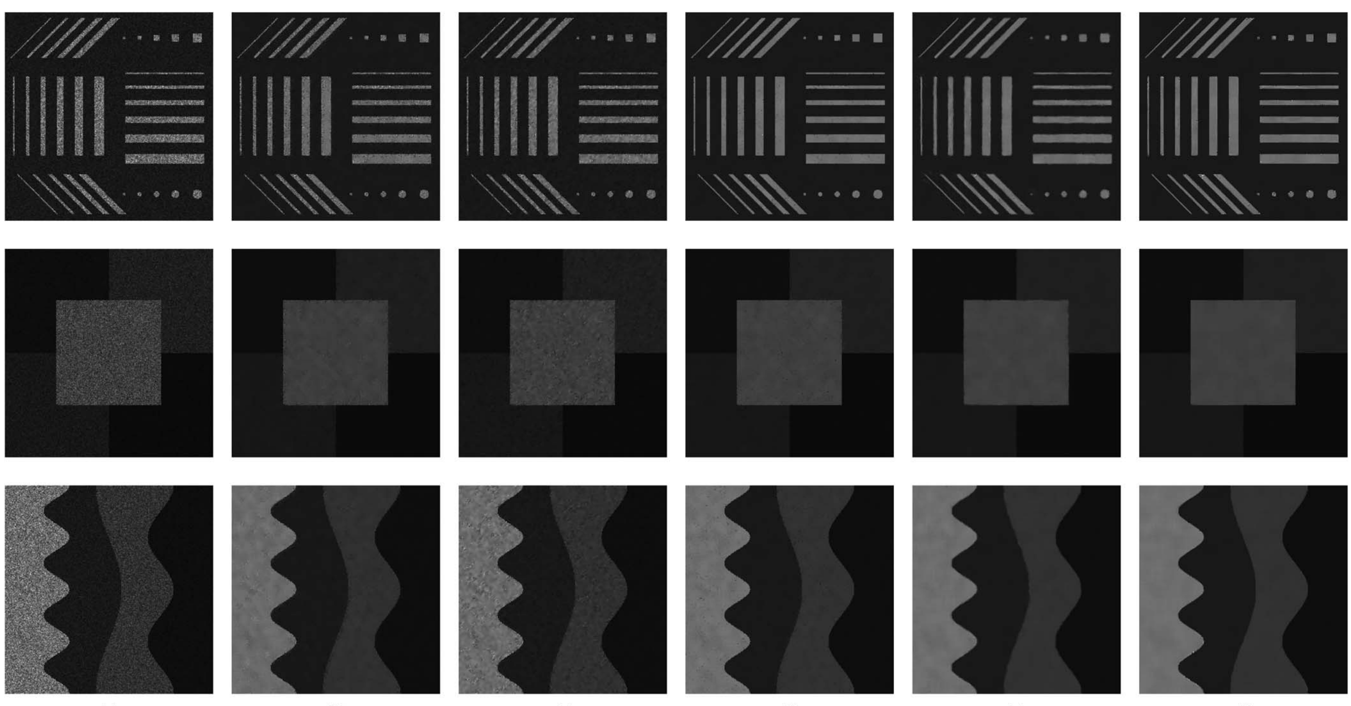

Fig. 7. Results of synthetic images that are corrupted with four-look speckle. The first column is the speckled images. From left to right are the results of (b) Refined Lee filter, (c) AKMMSE filter, (d) TSRG filter, (e) LHRS-PRM filter, and (f) Our proposed filter.

Lee filter, while the performance of our method is better than that of LHRS-PRM. In light of the aforementioned analysis, we can conclude that a better performance in terms of the speckle reduction and the persistence of details is obtained by our method.

B. Real SAR Images

In this section, four real SAR images are used for further analysis, which are the following: 1) Field [rural scene in Bedfordshire, X-band, 3-m resolution, 3.2-look [24], and shown as Fig. 8(a)]; 2) Town [town near Xi'an, China, 3-m resolution, four-look, and shown as Fig. 9(a)]; 3) Yellow River [estuary near Yellow River in China, C-band, 8-m resolution, four-look, and shown as Fig. 10(a)]; and 4) Horse Track [horse track near Albuquerque, NM, Ku-band, 1-m resolution, four-look, and shown as Fig. 11(a)]. The comparison methods and parameter settings are identical to that used in the experiments of synthetic images. The visual results are shown in Figs. 8–11. Since the underlying signal is hardly to be obtained for real SAR images, the numerical indexes calculated by using the images before and after filtering are used for analysis. In this paper, EPD-RoA [24], mean and variance of the ratio map between the speckled and despeckled images, and speckle looks

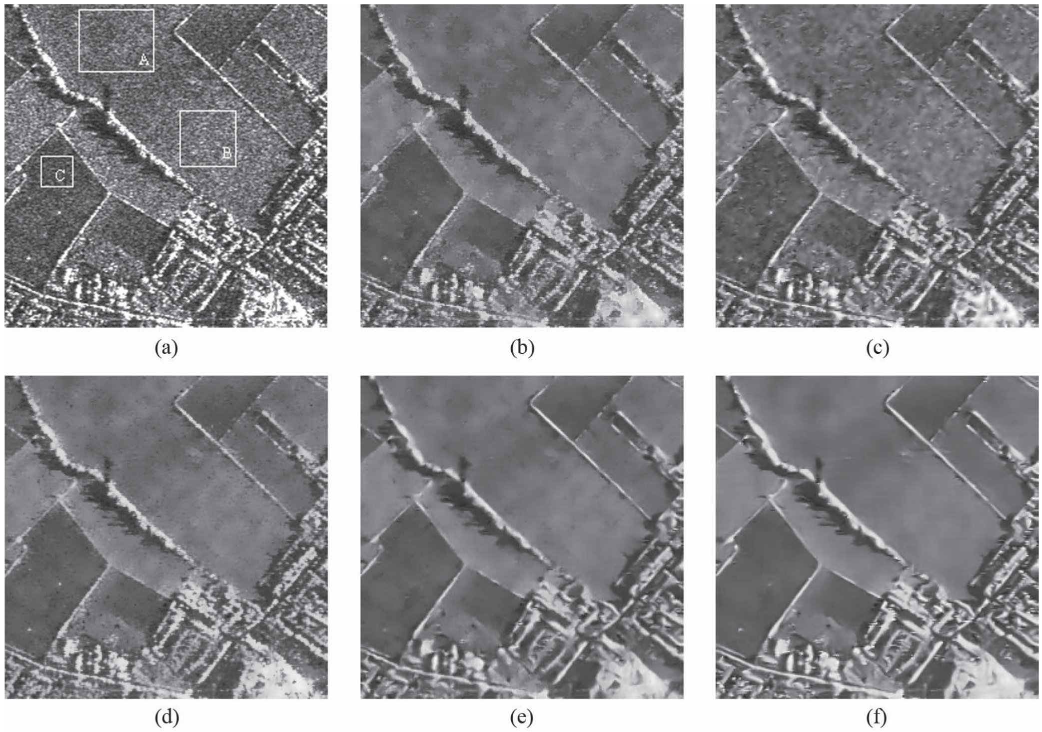

Fig. 8. Results of Field. (a) Original image. (b) Refined Lee filter. (c) AKMMSE filter. (d) TSRG filter. (e) LHRS-PRM filter. (f) Our proposed filter.

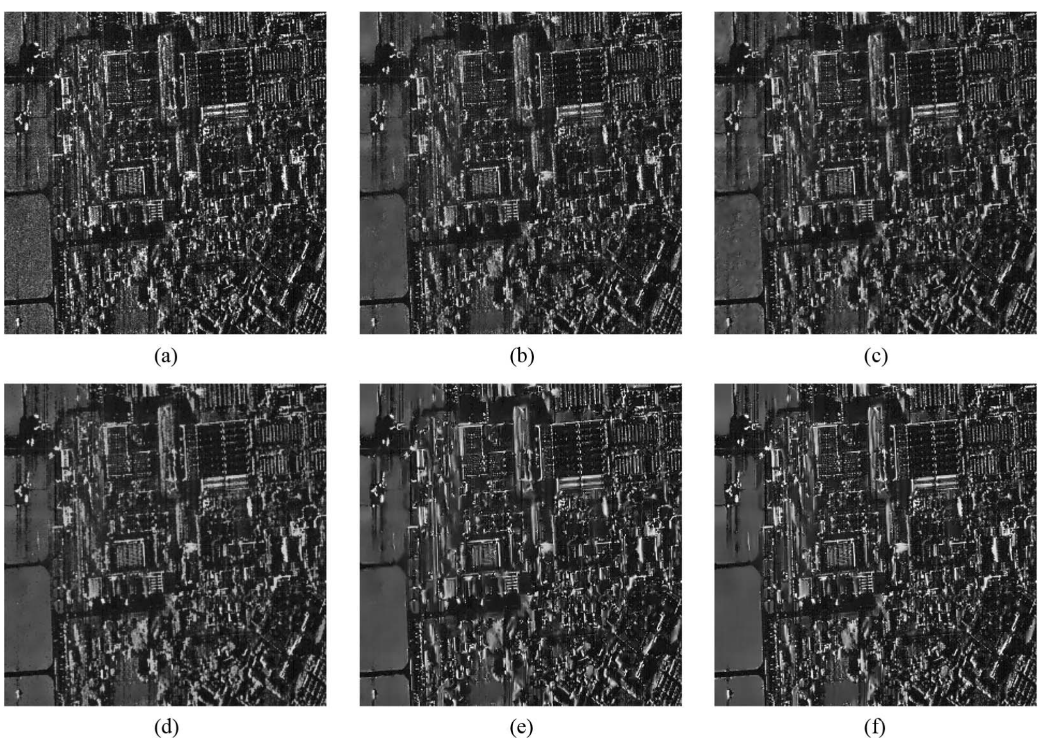

Fig. 9. Results of Town. (a) Original image. (b) Refined Lee filter. (c) AKMMSE filter. (d) TSRG filter. (e) LHRS-PRM filter. (f) Our proposed filter.

(SL) [37] are calculated in Table II. For a better analysis, the ideal values of these indexes are also given in the table. Moreover, equivalent number of looks (ENL) of several preselected larger homogeneous regions are calculated in Table III to evaluate the smoothing ability of different methods. It is noted that all real SAR images are 8-bit images.

In the visual results of the Refined Lee filter and AKMMSE filter shown as Fig. 8(b) and (c), some speckle residuals are observed, while the details of the image are well preserved, such as the point targets in the left-bottom part of Field. For the TSRG filter, some unexpected dark spots are clearly observed in the results, while the details are also well preserved, such as the

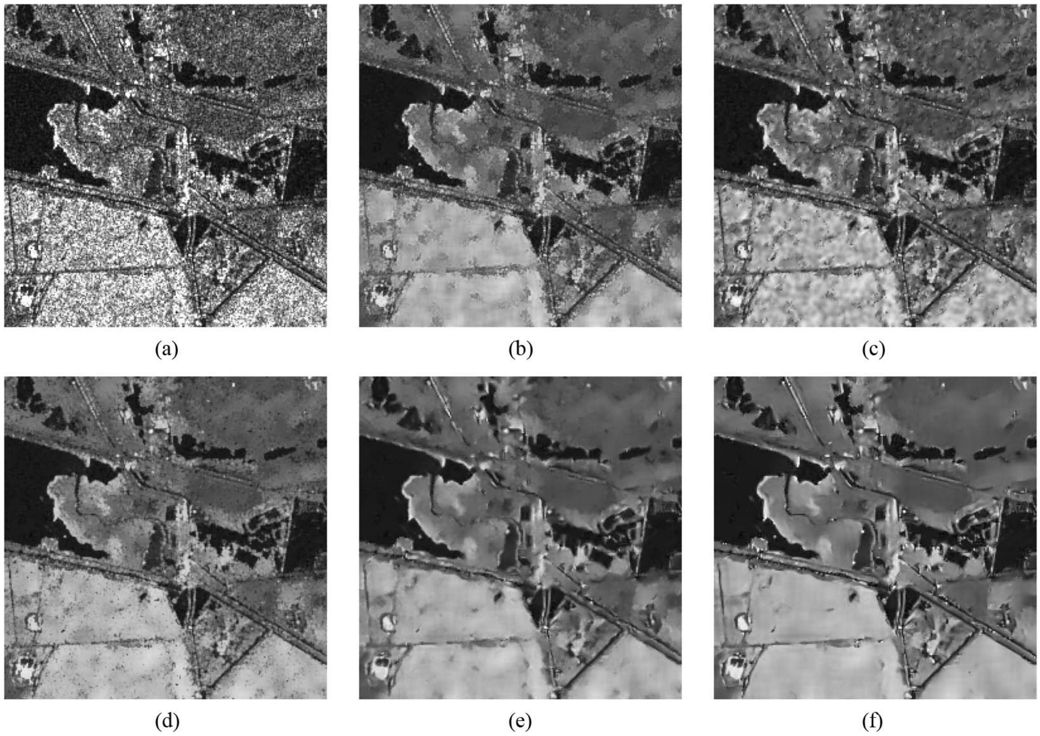

Fig. 10. Results of Yellow River. (a) Original image. (b) Refined Lee filter. (c) AKMMSE filter. (d) TSRG filter. (e) LHRS-PRM filter. (f) Our proposed filter.

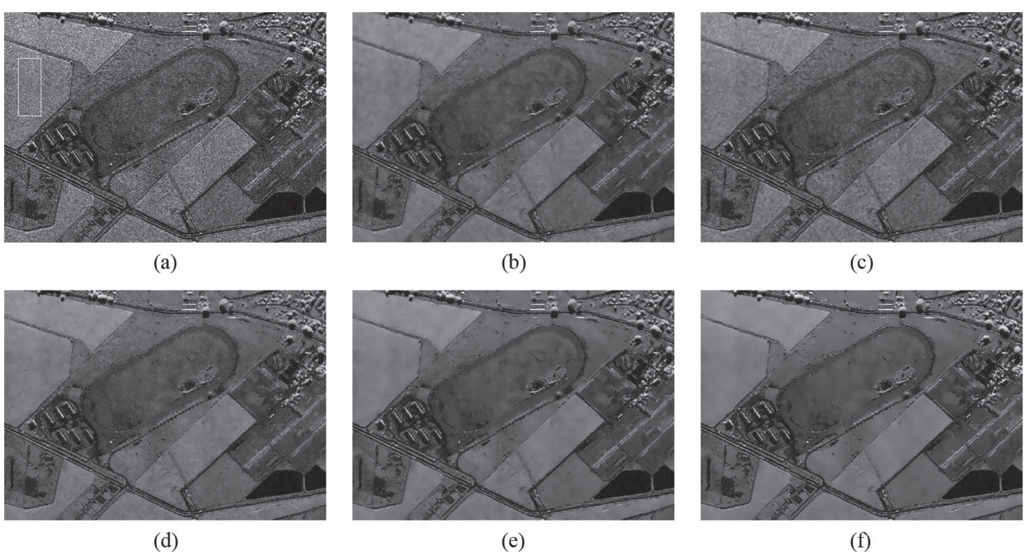

Fig. 11. Results of Horse Track. (a) Original image. (b) Refined Lee filter. (c) AKMMSE filter. (d) TSRG filter. (e) LHRS-PRM filter. (f) Our proposed filter.

left part of Horse Track [shown as Fig. 11(d)]. With the usage of neighborwise similar metric, the speckle is greatly suppressed in the results of the LHRS-PRM filter and our proposed filter. After careful observation, we can find that the profiles of some details of the image are enhanced and become clearer in the result of our method than in the result of the LHRS-PRM filter, such as the left-down part of Yellow River (shown in Fig. 10). The main reason is that the details are discriminated reasonably according to the extracted sketch map, and the directionality is analyzed and embodied in the similarity metric to determine the local maximal homogeneous region. Meanwhile, we can also find that the homogeneous regions of these tested images are smoother in the results of our method than in the results of other comparison filters, such as the left part of Town (shown in Fig. 9).

From the numerical indexes, some more conclusion is obtained. In terms of EPD-RoA, the highest value is achieved by our method in all SAR images except in Field and Yellow River for which the highest value is obtained by the AKMMSE filter. After a careful comparison, we can find that the details are well preserved by our method. Furthermore, the usage of the local geometrical property is better for the persistence of the details. This conclusion is consistent with that obtained from visual results. For the index of the mean of ratio map, a larger deviation is usually obtained by the TSRG filter, while a more reasonable result is attained by the LHRS-PRM filter. It means

TABLE II
NUMERICAL INDEXES FOR REAL SAR IMAGES

	Ratio Map		EPD-RoA		SL	Ratio Map		EPD-RoA		SL
	Mean	Variance	Horizontal	Vertical		Mean	Variance	Horizontal	Vertical	
	Field					Town				
Refined Lee	0.9851	0.0578	0.9509	0.9165	4.586	0.9458	0.0310	0.7490	0.7907	7.875
AKMMSE	0.9880	0.0365	**0.9532**	**0.9242**	7.296	**0.9664**	0.0215	0.8109	0.8256	11.892
TSRG	0.9398	0.0501	0.9482	0.9126	4.816	0.9003	0.0630	0.6445	0.6962	3.514
LHRS-PRM	**0.9790**	0.0862	0.9436	0.9054	**3.037**	0.9734	0.0638	0.8742	0.8841	**4.061**
Proposed	0.9368	0.0707	0.9461	0.9120	3.391	0.9841	0.0213	**0.9758**	**0.9771**	12.418
Ideal	**0.9594**	**0.0809**	**1.0000**	**1.0000**	**3.2**	**0.9693**	**0.0643**	**1.0000**	**1.0000**	**4**
	HorseTrack					YellowRiver				
Refined Lee	**0.9743**	0.0442	0.8886	0.8517	4.986	0.9820	0.0424	0.9275	0.9303	6.198
AKMMSE	0.9886	0.0263	0.9110	0.8961	7.762	0.9902	0.0271	**0.9362**	**0.9386**	9.832
TSRG	0.9367	0.0451	0.8770	0.8357	4.585	0.9436	0.0399	0.9225	0.9255	6.077
LHRS-PRM	0.9764	0.0684	0.9203	0.9091	3.416	**0.9769**	0.0753	0.9169	0.9190	3.458
Proposed	0.9613	0.0513	**0.9525**	**0.9516**	**4.285**	0.9502	0.0595	0.9317	0.9342	**4.140**
Ideal	**0.9693**	**0.0643**	**1.0000**	**1.0000**	**4**	**0.9693**	**0.0643**	**1.0000**	**1.0000**	**4**

TABLE III
NUMERICAL INDEX OF ENL

	Horse Track	Field(A)	Field(B)	Field(C)
Original	4.4541	2.9453	3.1628	2.6516
Refined Lee	76.8935	29.4693	49.6189	49.7054
AKMMSE	28.6969	12.0732	17.2586	10.1420
TSRG	64.2781	33.1958	61.1939	53.2173
LHRS-PRM	117.9687	50.8181	105.7774	159.4864
Proposed	**132.4105**	**70.2878**	**154.5343**	**309.4576**

TABLE IV
TIME CONSUMPTION FOR REAL SAR IMAGES

	Sketching process	Speckle reduction	Total
Field(256 × 256)	30.464s	20.622s	51.086s
Town(300 × 300)	43.609s	6.234s	49.843s
Yellow River(256 × 256)	30.127s	20.382s	50.509s
Horse Track(390 × 500)	106.518s	57.857s	164.375s

that the LHRS-PRM filter performs better on the preservation of scattering. From SL which is also computed from the ratio map, we can find that a better value is obtained by our method except for Town which contains many building scatters. However, due to the existence of many heterogeneous regions in Town, our method's performance in terms of SL is reasonable.

Since a better filtering method should perform well not only in the preservation of the details but also in the speckle reduction [15], some homogeneous regions [shown as Figs. 8(a) and 11(a)] are selected for evaluation. The calculated ENLs are recorded in Table III from which we can find that the highest value is obtained by our method. It means that the smoothing ability of our method is stronger than the rest, which can also be obtained from visual results. To sum up, a better performance is obtained by our method in terms of the preservation of the details and scattering and the speckle reduction.

C. Time Consumption

In this section, the time costs on four real SAR images are given in Table IV. It is noted that the results are obtained by nonoptimized C++ code implementing with Intel 3.2-GHz CPU and 4-GB memory PC. Since the sketch map is extracted in our method, the time consumption is a little expensive. For a better analysis, the time consumptions of different stages described in Section II (sketching process) and Section III (speckle reduction) are given, respectively, in Table IV. It is obvious that the time used for the sketching process is more than half of the total computation time. Moreover, the time used for the speckle reduction is related to the area of the homogeneous region. This can be obtained from the time consumption of Town in which the area of the heterogeneous region is larger.

V. CONCLUSION

In this paper, the sketch information of a SAR image has been extracted as the guidance for constructing the geometrical kernel function. Moreover, a modified ratio distance was developed to form a new neighborwise similarity metric. Since the local geometrical property is considered in the metric, more valid samples have been searched to estimate the underlying signal, especially for the details. Then, using the region growing method, a local adaptive region was obtained for each pixel, and the ML rule was used within the region for estimation. In the experiments of synthetic and real SAR images, it can be seen that, for our method, not only the speckle is greatly suppressed, but also the details are well preserved.

However, some parameters used to construct the geometrical kernel function are set empirically in our method. A data-driven selection method about these parameters will be our future work.

ACKNOWLEDGMENT

The authors would like to thank Prof. S. Yang of IIIP, Xidian University, Xi'an, China, and Prof. Y. Wu of the University of California, Los Angeles, CA, USA, for the useful discussions in developing the algorithm and the anonymous reviewers for their valuable suggestions which have helped in greatly improving this paper.

REFERENCES

[1] F. Fetter, D. Gineris, and J. Perbos, "Sea ice type map from Alaska synthetic aperture radar facility imagery: An assessment," *J. Geophys. Res.*, vol. 99, no. C11, pp. 22 443–22 458, Nov. 1994.
[2] J.-S. Lee, "Digital image enhancement and noise filtering by use of local statistics," *IEEE Trans. Pattern Anal. Mach. Intell.*, vol. PAMI-2, no. 2, pp. 165–168, Mar. 1980.
[3] D. T. Kuan, A. A. Sawchuk, T. C. Strand, and P. Chavel, "Adaptive noise smoothing filter for images with signal-dependent noise," *IEEE Trans. Pattern Anal. Mach. Intell.*, vol. PAMI-7, no. 2, pp. 165–177, Mar. 1985.
[4] V. S. Frost, J. A. Stiles, K. S. Shanmugan, and J. C. Holtzman, "A model for radar images and its application to adaptive digital filtering of multiplicative noise," *IEEE Trans. Pattern Anal. Mach. Intell.*, vol. PAMI-4, no. 2, pp. 157–166, Mar. 1982.
[5] A. Lopes, E. Nezry, R. Touzi, and H. Laur, "Maximum *a posteriori* speckle filtering and first order texture models in SAR images," in *Proc. 10th Annu. Int. Geosci. Remote Sens. Symp.*, Washington, DC, USA, May 1990, pp. 2409–2412.
[6] J.-S. Lee, "Refined filtering of image noise using local statistics," *Comput. Graphic Image Proc.*, vol. 15, no. 4, pp. 380–398, Apr. 1981.
[7] J.-S. Lee, J. Wen, T. Ainsworth, K. Chen, and A. Chen, "Improved sigma filter for speckle filtering of SAR imagery," *IEEE Trans. Geosci. Remote Sens.*, vol. 47, no. 1, pp. 202–213, Jan. 2009.
[8] J.-S. Lee, "Digital image smoothing and the sigma filter," *Comput. Vis., Graphics Image Process.*, vol. 24, no. 2, pp. 255–269, Nov. 1983.
[9] J. Park, W. Song, and W. Pearlman, "Speckle filtering of SAR images based on adaptive windowing," *Proc. Inst. Elect. Eng.—Vis., Image, Signal Process.*, vol. 146, no. 4, pp. 191–197, Aug. 1999.
[10] Y. Wu and H. Maître, "Smoothing speckled SAR images by using maximum homogeneous region filters," *Opt. Eng.*, vol. 31, no. 8, pp. 1785–1792, Aug. 1992.
[11] E. Trouve, J.-S. Lee, and V. Buzuloiu, "Intensity-driven adaptive-neighborhood technique for polarimetric and interferometric SAR parameters estimation," *IEEE Trans. Geosci. Remote Sens.*, vol. 44, no. 6, pp. 1609–1621, Jun. 2006.
[12] R. M. Rangayyan, M. Ciuc, and F. Faghih, "Adaptive-neighborhood filtering of images corrupted by signal-dependent noise," *Appl. Opt.*, vol. 37, no. 20, pp. 4477–4487, Jul. 1998.
[13] K. K. Gupta and R. Gupta, "Despeckle and geographical feature extraction in SAR images by wavelet transform," *ISPRS J. Photogramm. Remote Sens.*, vol. 62, no. 6, pp. 473–484, Dec. 2007.
[14] M. Amirmazlaghani and H. Amindavar, "A novel sparse method for despeckling SAR images," *IEEE Trans. Geosci. Remote Sens.*, vol. 50, no. 12, pp. 5024–5032, Dec. 2012.
[15] H. Xie, L. E. Pierce, and F. T. Ulaby, "SAR speckle reduction using wavelet denoising and Markov random field modeling," *IEEE Trans. Geosci. Remote Sens.*, vol. 40, no. 10, pp. 2196–2212, Oct. 2002.
[16] M. Walessa and M. Datcu, "Model-based despeckling and information extraction from SAR images," *IEEE Trans. Geosci. Remote Sens.*, vol. 38, no. 5, pp. 2258–2269, Sep. 2000.
[17] Y.-J. Yu and S. T. Acton, "Speckle reducing anisotropic diffusion," *IEEE Trans. Image Process.*, vol. 11, no. 11, pp. 1260–1270, Nov. 2002.
[18] P. Fatih, S. Rajagopalan, and S. Kei, "SAR despeckling by sparse reconstruction on affinity nets (SRAN)," in *Proc. 9th Eur. Conf. Synthetic Aperture Radar*, Apr. 2012, pp. 796–799.
[19] A. Buades, B. Coll, and J.-M. Morel, "A non-local algorithm for image denoising," in *IEEE Comput. Soc. Conf. Comput. Vis. Pattern Recogn.*, Jun. 2005, vol. 2, pp. 60–65.
[20] C. A. Deledalle, L. Denis, and F. Tupin, "Iterative weighted maximum likelihood denoising with probabilistic patch-based weights," *IEEE Trans. Image Process.*, vol. 18, no. 12, pp. 2661–2672, Dec. 2009.
[21] P. Coupe, P. Hellier, C. Kervrann, and C. Barillot, "Nonlocal means-based speckle filtering for ultrasound images," *IEEE Trans. Image Process.*, vol. 18, no. 10, pp. 2221–2229, Oct. 2009.
[22] H. Zhong, Y. W. Li, and L. C. Jiao, "SAR image despeckling using Bayesian nonlocal means filter with sigma preselection," *IEEE Geosci. Remote Sens. Lett.*, vol. 8, no. 4, pp. 809–813, Jul. 2011.
[23] O. D'Hondt, L. Ferro-Famil, and E. Pottier, "Nonstationary spatial texture estimation applied to adaptive speckle reduction of SAR data," *IEEE Geosci. Remote Sens. Lett.*, vol. 3, no. 4, pp. 476–480, Oct. 2006.
[24] H. X. Feng, B. Hou, and M. G. Gong, "SAR image despeckling based on local homogeneous region segmentation by using pixel relativity measurement," *IEEE Trans. Geosci. Remote Sens.*, vol. 49, no. 7, pp. 2724–2737, Jul. 2011.
[25] J. S. Lee and K. Hoppel, "Noise modeling and estimation of remotely sensed images," in *Proc. Int. Geosci. Remote Sens. Symp.*, Jul. 1989, vol. 2, pp. 1005–1008.
[26] D. Marr, *Vision*. New York, NY, USA: Freeman, 1982.
[27] C. E. Guo, S. C. Zhu, and Y. N. Wu, "Primal sketch: Integrating texture and structure," *Comput. Vis. Image Understanding.*, vol. 106, no. 1, pp. 5–19, Apr. 2007.
[28] R. Touzi, A. Lopes, and P. Bousquet, "A statistical and geometrical edge detector for SAR images," *IEEE Trans. Geosci. Remote Sens.*, vol. 26, no. 6, pp. 764–773, Nov. 1988.
[29] Z. Y. Bai, J. Yang, H. Liang, and W. L. Wang, "An optimal edge detector for bridge target detection in SAR images," in *Int. Conf. Commun., Circuits, Syst.*, May 2005, pp. 847–851.
[30] Y. Z. Zhang, H. J. Li, X. Wang, and W. Dan, "Edge extraction of marine oil spill in SAR images," in *Proc. Int. Conf. Challenges Environ. Sci. Comput. Eng.*, Mar. 2010, vol. 1, pp. 439–442.
[31] J. Liu and X. Mei, "Research on edge detection for SAR images," in *Proc. IEEE Int. Conf. Geosci. Remote Sens. Symp.*, Aug. 2006, pp. 3123–3126.
[32] F. Tupin, H. Maitre, J. F. Mangin, J. M. Nicolas, and E. Pechersky, "Detection of linear features in SAR images: Application to road network extraction," *IEEE Trans. Geosci. Remote Sens.*, vol. 36, no. 2, pp. 434–453, Mar. 1998.
[33] I. Bloch, "Information combination operators for data fusion: A comparative review with classification," *IEEE Trans. Syst., Man, Cybern., A, Syst., Humans*, vol. 26, no. 1, pp. 52–67, Jan. 1996.
[34] N. Otsu, "A threshold selection method from gray-level histograms," *IEEE Trans. Syst., Man, Cybern.*, vol. SMC-9, no. 1, pp. 62–66, Jan. 1979.
[35] J. Canny, "Finding Edges and Lines in Images," MIT, Cambridge, MA, USA, Tech. Rep. 720, 1983.
[36] Z. Wang, A. Bovik, H. Sheikh, and E. Simoncelli, "Image quality assessment: From error visibility to structural similarity," *IEEE Trans. Image Process.*, vol. 13, no. 4, pp. 600–612, Apr. 2004.
[37] J. Jian and C. Li, "SAR image despeckling based on bivariate threshold function in NSCT domain," *J. Electron. Inf. Technol.*, vol. 33, no. 5, pp. 1088–1094, 2011.

Jie Wu received the B.S. degree from Xidian University, Xi'an, China, in 2008, where he is currently working toward the Ph.D. degree in computer application technology in the School of Computer Science and Technology and the Key Laboratory of Intelligent Perception and Image Understanding of the Ministry of Education of China, Xi'an.

His current research interest is synthetic aperture radar image processing including despeckling and segmentation.

Fang Liu (M'07–SM'07) received the B.S. degree in computer science and technology from Xi'an Jiaotong University, Xi'an, China, in 1984 and the M.S. degree in computer science and technology from Xidian University, Xi'an, in 1995.

She is currently a Professor with the School of Computer Science, Xidian University. She is the author or coauthor of 5 books and more than 80 papers in journals and conferences. Her research interests include signal and image processing, synthetic aperture radar image processing, multiscale geometry analysis, learning theory and algorithms, optimization problems, and data mining.

Licheng Jiao (SM'89) received the B.S. degree from Shanghai Jiaotong University, Shanghai, China, in 1982 and the M.S. and Ph.D. degrees from Xi'an Jiaotong University, Xi'an, China, in 1984 and 1990, respectively.

He is currently a Distinguished Professor with the School of Electronic Engineering, Xidian University, Xi'an. He has led approximately 40 important scientific research projects and has published more than 10 monographs and 100 papers in international journals and conferences. He is the author of three books: *Theory of Neural Network Systems* (Xidian University Press, 1990), *Theory and Application on Nonlinear Transformation Functions* (Xidian University Press, 1992), and *Applications and Implementations of Neural Networks* (Xidian University Press, 1996). He is the author or coauthor of more than 150 scientific papers. His research interests include signal and image processing, natural computation, and intelligent information processing.

Prof. Jiao is a member of the IEEE Xi'an Section Executive Committee and the Chairman of the Awards and Recognition Committee and an executive committee member of the Chinese Association of Artificial Intelligence.

Hongxia Hao (M'11) received the B.S. degree from Xidian University, Xi'an, China, in 2003, where she is currently working toward the Ph.D. degree in computer application technology in the School of Computer Science and Technology and the Key Laboratory of Intelligent Perception and Image Understanding of the Ministry of Education of China, Xi'an.

Her current interests include multiscale geometric analysis and intelligent image processing.

Xiangrong Zhang (M'07) received the B.S. and M.S. degrees in computer science and technology and the Ph.D. degree in pattern recognition and intelligent system from Xidian University, Xi'an, China, in 1999, 2003, and 2006, respectively.

She is currently a Professor with the Key Laboratory of Intelligent Perception and Image Understanding of the Ministry of Education, School of Electronic Engineering, Xidian University. Her current research interests include image analysis and understanding, pattern recognition, and machine learning.

Shuang Wang (M'07) was born in Shannxi, China, in 1978. She received the B.S. and M.S. degrees and the Ph.D. degree in circuits and systems from Xidian University, Xi'an, China, in 2000, 2003, and 2007, respectively.

She is currently a Professor with the Key Laboratory of Intelligent Perception and Image Understanding of the Ministry of Education of China, Xidian University. Her main research interests are image processing, machine learning, synthetic aperture radar (SAR)/POL SAR image processing, etc.